Corrosion Science 258 (2026) 113333

Contents lists available at ScienceDirect

Corrosion Science

journal homepage: www.elsevier.com/locate/corsci

Investigating the role of grain boundary hydrogen in dual atmosphere effects for solid oxide cells interconnect applications

Gongmei Yang [a,b], Siqi Wang [a], Andrew Potter [a], Joy Sumner [a,*]

[a] Faculty of Engineering and Applied Sciences, Cranfield University, Bedfordshire, UK
[b] School of Material Science and Engineering, Jiangsu University, Zhenjiang, Jiangsu, China

ARTICLE INFO

Keywords:
Solid oxide fuel cells
Metallic interconnects
Dual atmosphere
Time-of-flight secondary ion mass spectrometry
First principle computation
Density functional theory

ABSTRACT

Ferritic stainless steel (FSS) is widely used as an interconnect material in solid oxide cells (SOCs). However, these interconnects degrade faster under simultaneous exposure to oxidizing and reducing atmospheres, a phenomenon known as the dual atmosphere effect. This study used SUS430 to investigate the mechanisms behind this effect. Oxidation behavior was compared for single air atmosphere, and dual atmosphere at 750 °C after 50, 100, and 200 h. Time-of-flight secondary ion mass spectrometry (ToF-SIMS) showed significant hydrogen enrichment at grain boundaries after 200 h in the dual atmosphere exposure as compared to the single atmosphere. To explore hydrogen's role, first-principles calculations were performed evaluating its adsorption energy on the (110) Fe–Cr crystal plane and its impact on Cr diffusion. The results revealed that hydrogen's presence raises the energy barrier for Cr diffusion and alters its pathway. This suggests that hydrogen enrichment at grain boundaries is a major factor in the dual atmosphere effect, as it hinders Cr diffusion, contributing to accelerated degradation of interconnect materials.

1. Introduction

Solid oxide cells (SOCs), including solid oxide fuel cells (SOFCs) and solid oxide electrolysis cells (SOECs), are key technologies in the global energy transition [1]. SOFCs generate electricity with highly efficiency and low carbon emissions [2], while SOECs enable green hydrogen production and energy storage [3]. Together, they support clean power generation and carbon neutrality. A vital component of SOCs is the interconnect, which links individual cells, conducts electricity, and separates gases under high temperatures [4]. Its performance and durability are critical to the efficiency and longevity of SOC systems, making it a focus of technological advancements for global deployment [5].

Ferritic stainless steel (FSS) is currently the most commonly used interconnect material due to its moderate oxidation resistance, good thermal compatibility with electrolyte materials, relatively low electrical resistivity, ease of formability and manufacturability, and low cost [6,7]. However, at the operating temperatures used by SOCs, FSS forms Cr_2O_3 scales with protective properties. Over time, the growth of these Cr_2O_3 scales, which have moderated conductivity, can lead to an increase in area specific resistance (ASR), the thickness of Cr_2O_3 scales needs to therefore be limited [8]. Secondly, Cr_2O_3 reacts with oxygen and water to form vapor phase hexavalent chromium, which ultimately deposits out, including on the cathode, hindering the electrochemically active sites and greatly reducing the cathode's catalytic performance [9,10]. By applying protective coatings, the growth rate of oxidized scales can be slowed down and the evaporation of chromium can be reduced [5,6,11].

A significant issue that demands attention is the dual atmosphere effect. Under the operating conditions of SOFCs and SOECs, when the interconnect devices are exposed to two different environments (Oxidizing air on the cathode side and a hydrogen-rich reducing environment on the anode side), an enhanced oxidation effect is observed on the air side of the interconnect devices [12–19]. The severity of these dual atmospheric effects varies greatly in different studies [13,17,20]. Alnegren et al. [17] found that at 600 °C, hydrogen accelerates the depletion of chromium, leading to severe oxidation. By contrast, at higher temperatures such as 800 °C, the rapid diffusion of chromium helps alleviate this effect. This is also seen by Kurokawa et al. [13] and Stygar et al. [20] at 800 °C where the dual atmosphere effect was negligible. They believe that thicker steel samples and pre-oxidation treatment to form a stable protective layer can slow down hydrogen permeation. Similarly, Goebel et al. [18] reported that pre-oxidation can serve as a barrier for hydrogen gas, helping to protect the oxide layer from damage. However, some studies present differing perspectives on the mechanism of hydrogen and the significance of the dual atmosphere

* Corresponding author.
E-mail address: jsumner@swin.edu.au (J. Sumner).

https://doi.org/10.1016/j.corsci.2025.113333
Received 20 June 2025; Received in revised form 17 September 2025; Accepted 18 September 2025
Available online 24 September 2025
0010-938X/© 2025 The Authors. Published by Elsevier Ltd. This is an open access article under the CC BY license (http://creativecommons.org/licenses/by/4.0/).

Table 1
Experimental conditions of SUS430 alloys at single atmosphere and dual atmosphere, % is by volume.

	Name	Atmosphere 1	Atmosphere 2	Exposure/heat time (h)	Temperature (°C)
Single Atmosphere (430 Single)	430 50 h	Air + 3% H_2O	Air + 3% H_2O	50	750
	430 100 h	Air + 3% H_2O	Air + 3% H_2O	100	750
	430 200 h	Air + 3% H_2O	Air + 3% H_2O	200	750
Dual Atmosphere (430 Dual)	430 50 h	Air + 3% H_2O	2.91% H_2 + 94.09% Ar + 3% H_2O	50	750
	430 100 h	Air + 3% H_2O	2.91% H_2 + 94.09% Ar + 3% H_2O	100	750
	430 200 h	Air + 3% H_2O	2.91% H_2 + 94.09% Ar + 3% H_2O	200	750

effect. Variations in experimental conditions, such as material composition and environmental factors, may also contribute to discrepancies in findings, highlighting the need for further investigation.

Although it has been confirmed that hydrogen diffuses from the fuel side to the air side and affects the oxidation process on the air side, the mechanism by which hydrogen causes the rupture of protective oxidation scales has not been determined. There are several explanations for this mechanism. Rufner et al. [14] suggested that the oxygen partial pressure (p_{O_2}) on the air side undergoes local changes due to the permeation of hydrogen gas. In contrast, Yang et al. [12] suggest that an increase in cation vacancy concentration in oxides accelerates the growth of oxide scales. Given that hydrogen can influence defect chemistry in oxides, it is important to consider whether it plays a role in this process. However, a recent study by Gunduz et al. [19] indicated hydrogen does not affect oxygen permeability or oxide scale growth but impedes Cr diffusion along grain boundaries, leading to Cr_2O_3 degradation, most severe at 600 °C. The effect occurs over the 500–800 °C range, though the critical hydrogen concentration is unclear. Cr^{3+} is impacted because it diffuses via cation vacancies, which hydrogen alters, while O^{2-} diffusion remains largely unaffected.

In contrast, Yang et al. [12] believe that an increase in the concentration of cation vacancies in oxides enhances the growth rate of scales. In a recent study, Gunduz et al. [19] suggested that hydrogen does not affect the permeability of oxygen and does not directly affect the growth of oxide scales. On the contrary, they believe that hydrogen can cause protective Cr_2O_3 scales to degrading due to reduced Cr transport along metal grain boundaries.

Previous studies have extensively explored the impact of hydrogen on the dual atmosphere effect, focusing primarily on the observation and analysis of oxide layer morphology [18,19,21,22]. While these investigations have proposed various hypotheses regarding hydrogen's role, they lack direct evidence of hydrogen presence at grain boundaries under dual atmosphere conditions and fail to address its influence on chromium diffusion from an atomic-scale perspective.

This study examines the oxidation behavior of SUS430 interconnects under single (air with 3 vol.% H_2O) and dual atmosphere conditions (2.91% H_2, 94.09% Ar with 3 vol.% H_2O) at 750 °C for 50, 100, and 200 h, with a focus on the oxide layer formed on the oxygen side. By comparing the oxide layers under these conditions, significant differences in morphology and composition were identified. Time-of-flight secondary ion mass spectrometry (ToF-SIMS) [23] analysis was employed to track hydrogen diffusion within the interconnects, providing insights into hydrogen distribution and its potential role in influencing oxidation processes.

To further investigate the atomic-scale mechanisms by which hydrogen affects chromium diffusion, Fe-17.5%Cr alloy was used as a model system, and Density Functional Theory (DFT) [24] calculations were performed. First, the adsorption energy of hydrogen on the grain boundary surface of the Fe–Cr alloy was calculated to confirm hydrogen's tendency to localize at grain boundaries. Subsequently, the climbing image nudged elastic band (CI-NEB) method [25] was employed to determine the diffusion energy barriers of chromium with and without hydrogen. Comparing these energy barriers provided a quantitative assessment of hydrogen's impact on chromium diffusion. These findings theoretically demonstrate hydrogen's role as a primary driver of the dual atmosphere effect, offering valuable guidance for improving the durability and performance of SOCs metallic interconnects in industrial applications.

2. Experimental

2.1. Preparation of sample and exposure condition

The SUS430 stainless steel (Bare Fe, 16.00–18.00 wt% Cr, 1.00 wt% Mn, 0.75 wt% Si, 0.12 wt% C, 0.06 wt% Ni, 0.04 wt% P, 0.03 wt% S [26,27]) circular plate, with a diameter of 14 mm and a thickness of 3 mm, was used as a sample in this experiment. After ultrasonic cleaning, surface stains and impurities were removed using alcohol and acetone.

A high-temperature dual atmosphere test bench was specifically designed to ensure that both sides of the sample were exposed to humid oxygen and hydrogen during high-temperature testing. High-temperature ceramic sealing adhesive (Aremco Ceramabond 552) was applied to ensure airtightness during the testing process. For the air environment, compressed air mixed with 3 vol.% H_2O was supplied at an intake rate of 80 mL min^{-1}. On the hydrogen side, argon gas mixed with 2.91 vol.% hydrogen and 3 vol.% H_2O was used, with an intake rate of 10 mL min^{-1}. The details are shown in Table 1. The selection of the gas composition and gas flow was based on the research of Alnegren et al. [28]. The compressed gases were provided by BOC Ltd. The exposure temperature was set to 750 °C, with exposure durations of 50, 100, and 200 h, respectively.

In real-world applications, the air stream typically contains water vapor, originating from ambient humidity and the oxidation products of hydrogen fuel [29,30]. Water vapor undergoes partial thermal decomposition ($H_2O \rightleftharpoons H_2 + {}^1/_2O_2$). Our thermodynamic equilibrium calculations for a 97% Air + 3% H_2O atmosphere at 750 °C demonstrate that the resulting hydrogen partial pressure is extremely low, reaching only 1.33×10^{-11} atm [31]. Given this exceedingly low value, we conclude that the hydrogen generated from this decomposition is present in a minimal amount. This thermodynamically confirms that its reducing effect is insignificant in such an oxidizing atmosphere.

2.2. Composition and structural characterization

After exposure, the samples were cut into cross-sections and polished. Morphological and cross-sectional analyses of the samples were performed using a field-emission scanning electron microscope (FE-SEM, TESCAN VEGA 4) equipped with energy-dispersive X-ray spectroscopy (EDS, Oxford Instruments). The phase structures of the metal and oxide layers were characterized using X-ray diffraction (XRD, SIEMENS D500D) with Cu Kα radiation. Data were collected over a 2θ range of 20–80°, with a step size of 0.05°.

2.3. Tof-SIMS measurements

The grain boundaries of the cross-sectioned sample were exposed by swabbing the surface with Kaling's No. 2 etchant (5 g copper chloride, 100 mL hydrochloric acid, and 100 mL ethanol) for 30 s.

Time-of-flight secondary ion mass spectrometry (ToF-SIMS) has been widely used to study high-temperature oxidation mechanisms in metals [32] and corrosion processes in engineering alloys [33–35]. In our work, ToF-SIMS measurements were performed at Cranfield University using a TESCAN SOLARIS X microscope with a dual-beam

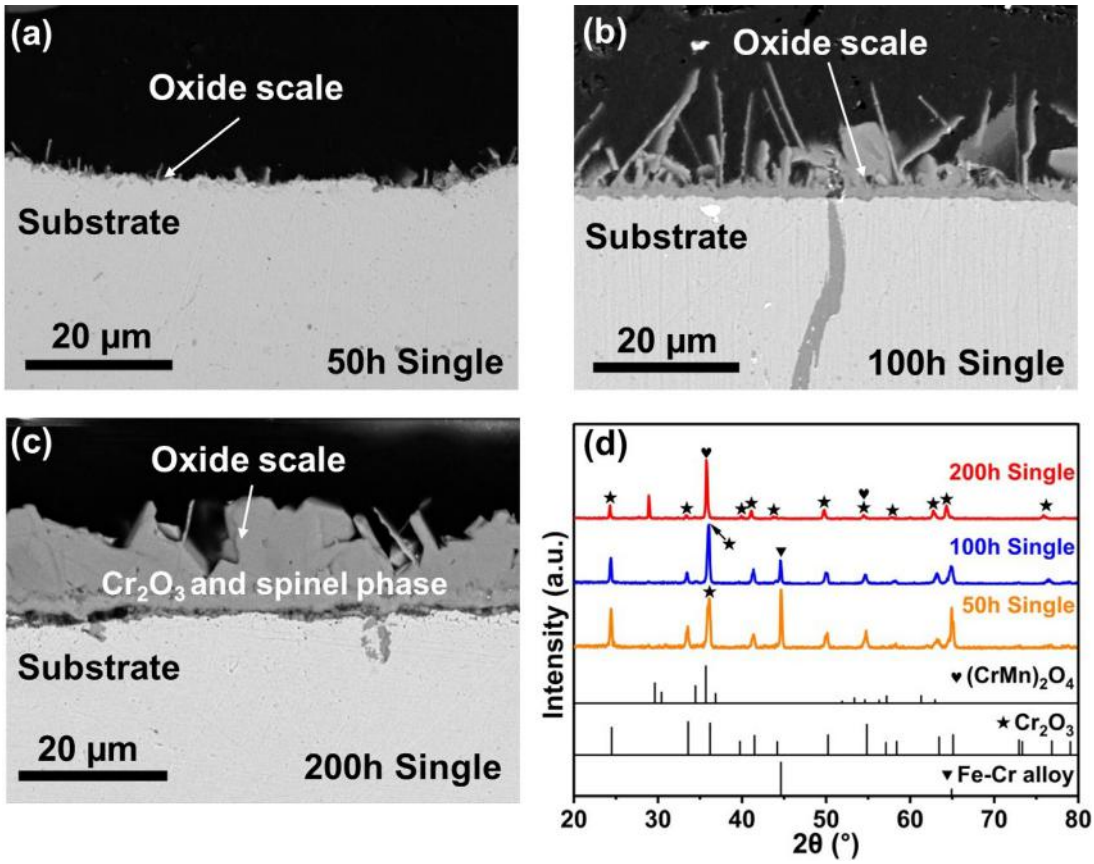


Fig. 1. SEM cross-section of SUS430 in cathode side exposed to the single atmosphere (air with 3% H_2O) at 750 °C for 50 h (a), 100 h (b), and 200 h (c), along with corresponding surface XRD analysis (d). XRD analysis phase identification used Powder Diffraction Files (PDF): Fe–Cr alloy (PDF #00-054-0031), Cr_2O_3 (PDF #01-070-3755) and $(CrMn)_2O_4$ (PDF #00-045-0504).

Table 2
The comparison of the thickness between the entire oxide scale, the protective oxide scale, and the oxide scale in the literature.

Exposure time (h)	Entire oxide scale (μm)		Protective oxide scale (μm)		Protective oxide scale in Ref. [36] (μm)
	Single	Dual	Single	Dual	Single
0	0	0	0	0	0
50	2.30	6.49	0.15	0.50	0.54
100	7.80	10.48	1.50	1.64	1.08
200	19.80	37.04	1.80	1.67	2.16
k_p ($\mu m^2\ s^{-1}$)	–	–	3.91×10^{-6}	4.30×10^{-6}	3.0×10^{-6}
Error	–	–	0.15	0.08	–

system containing the Triglav immersion optics column and the integrated Focused Ion Beam with xenon plasma (iFIB + Xe) optics column, all housed within a single chamber. This system combines the imaging capabilities of a scanning electron microscope (SEM) with the ability to perform surface modifications using a focused ion beam (FIB). High-precision elemental composition data were obtained with a mass resolution of 6000. The ion beam could be focused to 1–2 μm. Negative ion signals were collected, and the sputtering area was 20 μm × 20 μm. The FIB dwell time was 12 μs, and the number of frames was 320.

2.4. DFT calculation

The DFT calculations in this work were performed using the Quantum ESPRESSO software package [37]. A supercell containing 33 iron (Fe) atoms and 7 chromium (Cr) atoms was constructed to simulate the properties of the Fe-17.5%Cr alloy. The electronic configurations of Cr and Fe were set as Cr $3d^54s^1$ and Fe $3d^64s^2$. The generalized gradient approximation (GGA) with the Perdew–Burke–Ernzerhof (PBE) functional was used to model electron–ion interactions and describe exchange–correlation effects. The spin-polarization effect was included to account for the magnetic properties of the elements. Convergence tests were carried out, and the plane-wave cutoff energy was set to 350 electron volts (eV) along with a 2 × 2 × 5 Monkhorst–Pack k-point grid, achieving total energy errors below 10^{-6} eV per atom. For geometry optimizations, the threshold for force convergence was set to 0.001 eV/Å. For Cr diffusion, the nudged elastic band (NEB) method [38] was used to identify the minimum-energy pathway. Subsequently, the climbing-image nudged elastic band (CI-NEB) method was applied to refine the pathway, ensuring that the maximum force on each atom was reduced to below 0.01 eV/Å. This approach allowed for the accurate determination of the diffusion energy barrier associated with Cr diffusion.

3. Results and discussion

3.1. Oxidation in a single atmosphere

Fig. 1(a)–(c) show the microstructure of the entire oxide scales of the bare material SUS430 exposed to air with 3% H_2O at 750 °C for

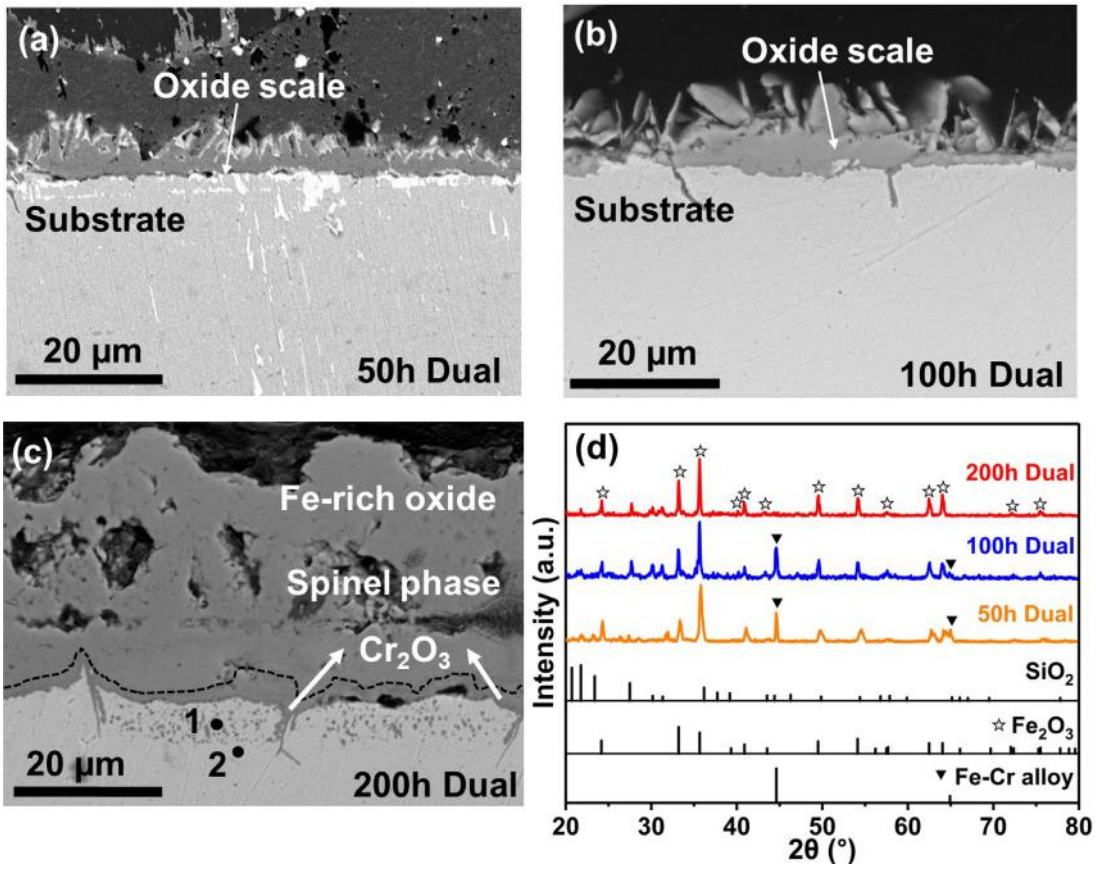


Fig. 2. SEM cross-section of SUS430 in cathode side exposed to the dual atmosphere (one side in air with 3% H_2O; the other side in 2.91% H_2, 94.09% Ar with 3% H_2O) at 750 °C for 50 h (a), 100 h (b), and 200 h (c), along with corresponding surface XRD analysis (d). XRD analysis phase identification used PDF cards: Fe–Cr alloy (PDF #00-054-0031), Fe_2O_3 (PDF #01-089-0599) and SiO_2 (PDF #00-042-1401).

50 h, 100 h, and 200 h, respectively. At this temperature, the metal elements on the surface of the alloy react with oxygen, and an uneven, thin oxide layer was found after 50 h of exposure. With continuous exposure to oxygen, the oxide grew thicker, with a microstructure which was characterized by the presence of two distinct layers, a denser oxide layer close to the substrate and an external 'flaky' oxide, as shown in Fig. 1(b). This high aspect ratio morphology of the lamellar crystals may be due to the presence of compressive stresses or dislocations inside the oxide during the growth process; these both promote the rapid diffusion of cations in an axial direction parallel to the scale surface [39–41]. After 200 h of exposure, the thickness of the entire oxide scale is about 19.8 μm, and the scale appears dense and adherent, with no visible gaps or significant defects. The compact nature of the scale, combined with the lack of internal oxidation or porosity, indicates that the single atmosphere promotes the formation of a protective and continuous oxide layer that inhibits further corrosion. However, a small amount of flaky oxide remains on the surface. The oxide composition of the formed layers was further investigated by XRD in Fig. 1(d). All spectra show the presence of Cr_2O_3, but the substrate peak of Fe–Cr alloy gradually weakens with increasing oxide layer, and is hardly observed after 200 h of exposure. The peak of the Cr_2MnO_4 spinel phase becomes more pronounced after 200 h of exposure, which is similar findings reported by Spotorno et al. [42]. As the oxide layer thickens, the intensity of the chromium and spinel peaks increases. In addition to the Cr_2MnO_4 spinel, the $CrMnFeO_4$ spinel phase may also form. This is expected, as the manganese and iron contained in the alloy can diffuse through Cr_2O_3 and form spinel on the outer surface of the oxide [43]. The second peak in the 200 h single-atmosphere spectrum ($2\theta = 28.9°$) corresponds well in position to the main peak of SiO_2 (refer to the SiO_2 peak in Fig. 2d). This SiO_2 signal originates from slight volatilization of the high-temperature ceramic sealant used in the experimental setup, which contains SiO_2.

3.2. Oxidation in dual atmosphere

Fig. 2(a)–(c) show the air-side oxide microstructure on SUS430 exposed to a dual atmosphere after 50 h, 100 h, and 200 h, respectively. The thickness of the oxidation scale in single- and dual-atmosphere conditions is shown in Table 2. Note: The oxide thickness reported here includes the height of outermost whiskers, representing total surface damage.

After 50 h of exposure, the oxide layer thickness is approximately 6.5 μm, which is thicker and more uniform compared to the oxide formed in a single atmosphere. The surface exhibits a jagged morphology. This structure could be related to compressive stress or dislocations within the oxide layer, as previously mentioned for the oxide grown in a single atmosphere. Over time, the oxide layer thickens from 6.5 to 10.4 μm, retaining flake- or whisker-like structures on the surface due to compressive stress or dislocations. Additionally, internal corrosion may occur, leading to crack-like corrosion inside the SUS430 substrate, as shown in Fig. 2(b). After 100 h of exposure, the entire oxide scale in the dual-atmosphere condition (approximately 10.4 ± 2 μm) is overall thicker than that in the single-atmosphere condition (approximately 7.8 ± 2 μm).

Table 2 is provided to distinguish between the entire oxide scale and the protective oxide scale. Moreover, the calculated parabolic rate constants (k_p) are compared with literature values to objectively evaluate the oxidation kinetics. The calculated k_p values were found to be 3.91×10^{-6} μm^2 s^{-1} in a single atmosphere and 4.3×10^{-6} μm^2 s^{-1} in a dual atmosphere. These results are consistent with the kp value of

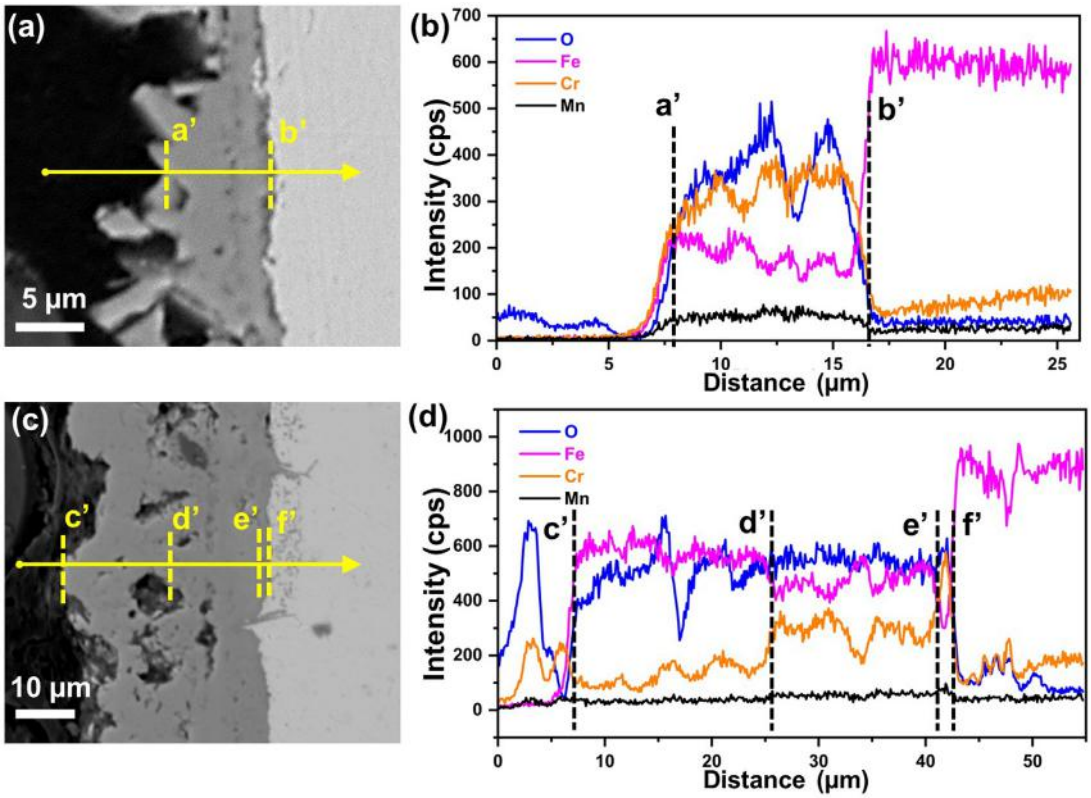


Fig. 3. SEM cross-section of SUS430 in cathode side exposed to the single atmosphere at 750 °C for 200 h (a) and the line scan. (b) SEM cross-section of SUS430 exposed to the dual atmosphere at 750 °C for 200 h (c) and the line scan (d).

3.0×10^{-6} μm^2 s^{-1} reported by Brylewski et al. [36] for SUS430 alloy. The agreement between the values confirms that the oxidation kinetics observed in the present work are consistent with previously established studies, indicating typical oxidation behavior under the investigated conditions.

After 200 h of exposure, the average oxide layer thickness reaches approximately 37 ± 3 μm, with voids or pores observed. The formation of these voids is likely a consequence of the degradation of the underlying Cr_2O_3 scale. In high-temperature environments, especially under dual-atmosphere conditions with water vapor, the protective Cr_2O_3 scale can undergo volatile degradation by forming gaseous $CrO_2(OH)_2$ species [44]. This process disrupts the dynamic equilibrium between scale growth and evaporation. If the evaporation rate exceeds the formation rate, micro-voids can initiate within the Cr_2O_3 layer or at its interface with the alloy [17,44]. These defects subsequently act as nucleation sites for larger voids. Furthermore, they compromise the protectiveness of the chromia layer, facilitating the outward diffusion of iron cations (Fe^{2+}). The outward-growing iron-rich spinel layer then encapsulates and amplifies these initial defects, leading to the macroscopic pores observed within the spinel matrix. While the outward diffusion of metal cations can also contribute to void formation via the Kirkendall effect [28,45], the mechanism linked to chromium volatility is considered dominant in this case, as it directly correlates with the conditions that lead to protective scale breakdown and Cr depletion. Moreover near the substrate, in addition to crack-like Cr_2O_3 formations, point-like elemental enrichments are observed in the substrate material, as shown in Fig. 2(c). EDS analysis indicates that these point-like enrichments are also Cr_2O_3, as shown in Table 3.

In high-temperature oxidation or corrosion environments, oxygen diffuses into the metal or alloy and reacts with specific active elements, forming an internal oxidation zone (IOZ) [46]. Internal oxidation is primarily driven by oxygen diffusion and the selective oxidation of alloying elements [47]. Since these oxides do not form a continuous protective layer, they exist instead as dispersed particles, as shown in Fig. 2(c). These oxide particles may be distributed along grain boundaries, within grains, or in a finely dispersed state at the nanoscale to submicron scale. Over time, oxygen continues to diffuse and react with deeper regions of the metal, which may cause the IOZ to gradually extend further into the material. The exact distribution of these oxide particles, that is, whether they are located between grains or inside grains, could be further investigated in future work using transmission electron microscopy.

Table 3
EDS spectra data from points in Fig. 2(c).

Spectrum (wt.%)	Point 1	Point 2
Fe	63.11	82.61
Cr	15.22	5.99
O	10.61	b.d.l.(<0.5)
C	7.88	8.33
Si	0.23	0.12
Au	2.91	2.95
Total	100.00	100.00

Note: Spectrum point 1 is located in the dark-colored elemental enrichment region, while spectrum point 2 is in the light-colored area. b.d.l. indicates below the detection limit. The detection limit for oxygen is approximately 0.5 wt%.

The oxide layer appears more irregular and disrupted compared to the single atmosphere. The entire oxide scale appears to consist of three distinct layers: an outer layer of Fe_2O_3, a middle spinel phase of $(Fe,Cr)_3O_4$ [48,49], and an inner layer of Cr_2O_3 adjacent to the substrate. The prominent presence of iron oxides suggests that the outward diffusion of Cr within the interconnect may be inhibited for some reason, resulting in an increased outward diffusion of Fe, potentially occurring simultaneously.

The oxide layer composition was further investigated using XRD, as illustrated in Fig. 2(d). In contrast to the XRD results (Fig. 1(d))

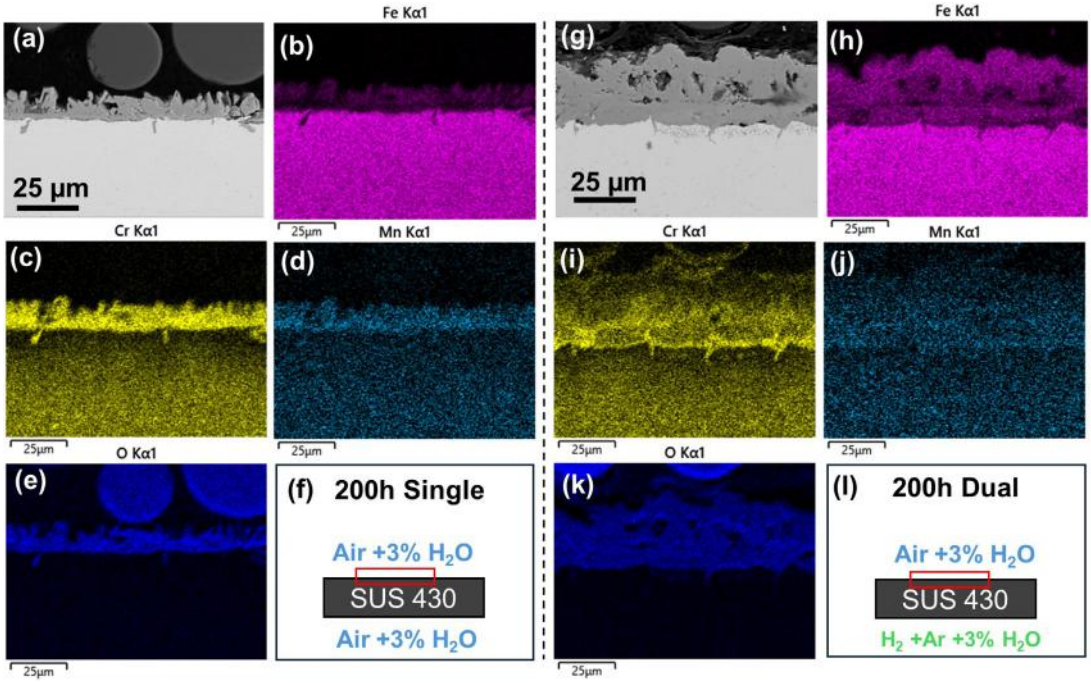


Fig. 4. SEM cross-section of SUS430 in cathode side exposed to the single atmosphere at 750 °C for 200 h (a) and the EDS maps (b–e), and schematic illustration of the single atmosphere test. (f) SEM cross-section of SUS430 exposed to the dual atmosphere at 750 °C for 200 h (g) and the EDS maps (h–k), and schematic illustration of the dual atmosphere test (l).

under single-atmosphere conditions, Fe_2O_3 emerged as the predominant phase, while peaks corresponding to the bare Fe–Cr alloy were also identified. However, with the progressive thickening of the oxide layer, the intensity of the Fe–Cr alloy peaks diminished and became nearly undetectable after 200 h of exposure. It is important to note that high-temperature ceramic adhesives, primarily consisting of SiO_2 [50], were employed during the dual-atmosphere experiments to ensure gas tightness. Upon sample retrieval post-exposure, adhesive particles may have detached and deposited onto the sample surface, potentially introducing impurities that contributed to elevated noise levels in the XRD spectra.

3.3. Comparison between single atmosphere and double atmosphere

To better compare the differences in the oxide layer on the air side under single and dual atmospheres, line scans (as shown in Fig. 3) and mapping (as shown in Fig. 4) were performed for samples exposed at 750 °C for 200 h in single and dual atmospheres.

The SEM images of the single atmosphere sample in Fig. 3(a)–(b) show that the oxide layer is relatively evenly distributed between the substrate and the outer surface. The corresponding line scan in Fig. 3(b) reveals that the oxygen concentration sharply increases at the surface (a′) and remains stable, indicating that the oxide layer is predominantly concentrated near the surface. The Fe concentration decreases within the oxide layer (a′ to b′), while Cr and Mn show some variation in distribution, with Cr being somewhat enriched within the oxide layer.

In contrast, the SEM images of the dual atmosphere sample in Fig. 3(c)–(d) reveal a distinctly layered structure in the oxide layer, with different oxidation behaviors observed near the outer and inner surfaces. The line scan in Fig. 3(d) shows that Fe has a high concentration near the outer surface (c′ to d′), slightly decreases in the middle layer (d′ to e′), and further drops near the interface between the oxide layer and the substrate (e′ to f′). Conversely, Cr exhibits the opposite trend, with low concentrations at the outer surface, increasing in the middle layer, and becoming significantly enriched near the oxide-substrate interface, potentially forming a protective Cr_2O_3 layer [17,19,28]. The Mn concentration, on the other hand, shows no significant variation within or outside the oxide layer. The occasional sharp drops in the oxygen signal (e.g., between c′ and d′ in Fig. 3(d)) are artifacts caused by the line scan traversing microscopic pores within the oxide layer, as evidenced by the dark contrast in the corresponding SEM image (Fig. 3(c)).

Based on the variations in Fe and Cr concentrations, the oxide layer under dual atmosphere conditions can be divided into three distinct layers: a Fe-rich outer layer (c′ to d′), a Fe–Cr mixed middle layer (d′ to e′), and a Cr-rich inner layer (e′ to f′) near the substrate interface. This structure is consistent with findings reported in the literature [17,19,28]. The complex oxide formation process observed in dual atmospheres is likely influenced by the diffusion of oxygen and the interaction with the reducing atmosphere, resulting in more intricate oxide layer formation mechanisms.

Combining the line scans and mapping analysis of this study with the results obtained by Alnegren et al. [17] using TEM, the outward growing Fe_2O_3 layer $(Fe, Cr)_3O_4$ layer growing inward beneath Fe_2O_3 layer, and a continuous Cr_2O_3 band coated with $(Fe, Cr)_3O_4$ layer on the metal oxide interface. The innermost region of this area consists of a mixture of metal and oxides, with the primary oxide component being Cr_2O_3 [28,45,51]. This phenomenon has also been reported in other studies. According to Pujiaksono et al. [51], this metal/oxide mixture may result from immiscibility gaps in the Fe–Cr–O spinel phase system.

Compared to the oxide layer on the air side under single atmosphere conditions, the most notable difference in the dual atmosphere oxide layer is the growth of hematite (Fe_2O_3). The formation of this iron oxide is detrimental for interconnect applications because the growth rate of iron oxides is several orders of magnitude faster than that of chromium oxides, resulting in poor corrosion protection performance [52]. The breakaway oxidation of iron oxides tends to initiate at one or a few localized points and then spread laterally, rather than occurring uniformly across the entire sample surface [53].

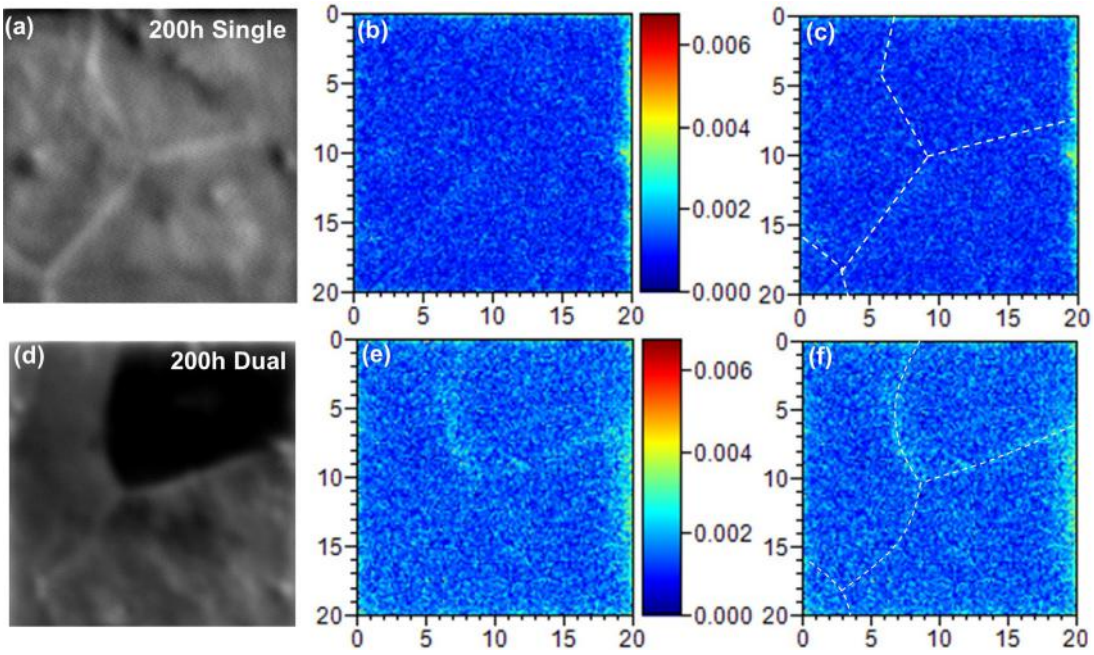


Fig. 5. Plane-view ToF-SIMS analysis of polished samples after exposure at 750 °C for 200 h under the single atmosphere (a–c) and the dual atmosphere (d–f). The two-dimensional distribution of hydrogen concentration is shown for the single atmosphere in (b), with grain boundaries highlighted by dashed lines in (c). Similarly, the two-dimensional hydrogen distribution under the dual atmosphere is presented in (e), with grain boundaries highlighted by dashed lines in (f). The field of view is 20 μm × 20 μm. (For interpretation of the references to color in this figure legend, the reader is referred to the web version of this article.)

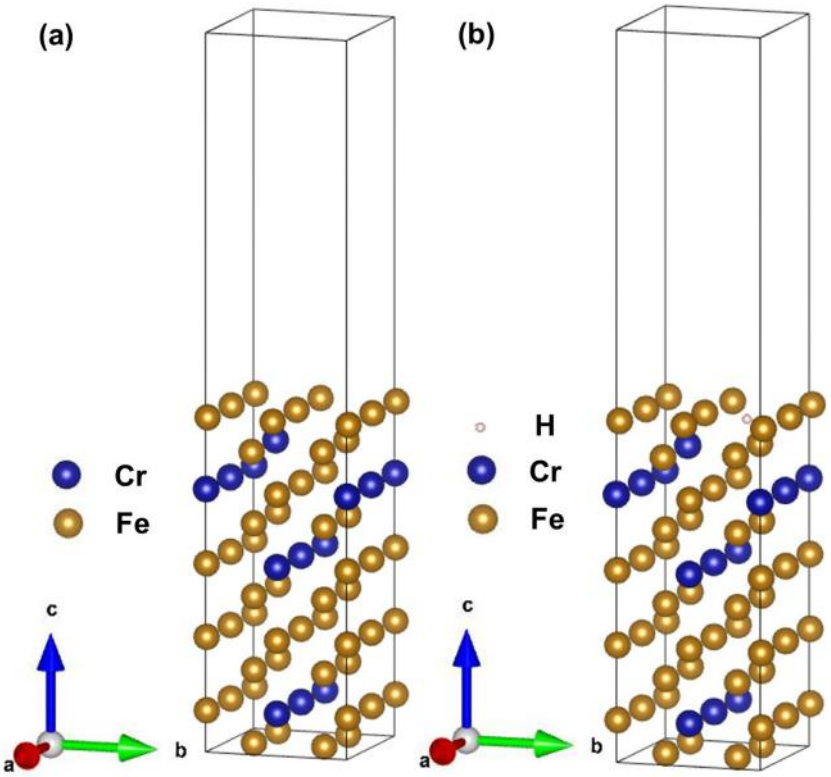


Fig. 6. Schematic diagram of Fe33Cr7 supercell (a) and the same structure after hydrogen adsorption (b) in the (110) crystal plane.

The formation of Fe_2O_3 is associated with the evaporation of the protective Cr_2O_3 layer and the presence of water vapor. At the interface between the substrate material and the oxide layer, a distinct chromium-enriched layer is observed, with a tendency to extend inward [15,54]. This observation is supported by the inward-extending cracks and localized chromium enrichment shown in Fig. 2c. Firstly, when water vapor reaches the interface between the metal and the oxide layer, it forms an H_2–H_2O redox atmosphere [55]. This redox environment alters the oxygen transport mechanism, accelerating the diffusion of oxygen anions (O^{2-}) into the substrate. Under such

conditions, further oxidation of the substrate proceeds with minimal resistance from the oxide layer. Secondly, the protective Cr_2O_3 layer in the oxide scale reacts with water vapor to form hydroxides, which gradually volatilize as $CrO_2(OH)_2$ [44]. The chemical reaction is as follows:

$$Cr_2O_3(s) + \frac{3}{2}O_2(g) + 2H_2O(g) \rightarrow 2CrO_2(OH)_2(g) \quad (1)$$

As the Cr_2O_3 layer continues to volatilize, it becomes thinner, and its oxidation resistance significantly declines [56]. At the same time, numerous voids and cracks form within the Cr_2O_3 layer, further facilitating the outward diffusion of iron cations (Fe^{2+}) and the inward diffusion of oxygen anions (O^{2-}) [57]. In the chromium-depleted regions, a non-protective oxide, $(Fe, Cr)_3O_4$, forms [19,28,58]. Since the mobility of Fe ions is higher than that of Cr ions, Fe ions preferentially migrate outward and react with oxygen at the surface, forming an iron-rich outer oxide layer [59].

During this process, Fe_2O_3 is believed to grow outward and laterally, gradually eroding and dissolving the original Cr_2O_3 layer. As the chromium oxide layer becomes increasingly iron-rich and loses its protective properties, breakaway oxidation subsequently initiates in the next alloy grain, further accelerating oxidation and corrosion [17,19,28].

Fig. 4 provides a schematic illustration of the single atmosphere (f) and dual atmosphere (l). The EDS maps provide two-dimensional spatial distribution of key elements, offering complementary evidence to the line scans (Fig. 3) for delineating the distinct layered structure of the oxide scale. The only difference between the two conditions is the presence of hydrogen on the fuel side, so we hypothesize that hydrogen is the main cause of the dual atmosphere effect. Additionally, hydrogen can diffuse through the stainless steel substrate, with a permeation rate of approximately 0.0126 $cm^2\ s^{-1}$ at 750 °C [60]. However, how hydrogen permeation specifically affects the properties of the oxide layer on the air side remains unclear. Some studies suggest that hydrogen may be absorbed into the oxide layer in the form of hydroxide ions, creating defects that could increase the outward diffusion rate of metal ions [12]. If this is the case, the thickness of the protective chromia (Cr_2O_3) layer formed under dual-atmosphere conditions would be expected to be greater than that formed under single-atmosphere conditions. However, in this study, no significant difference in oxide layer thickness between the dual and single atmosphere conditions could be distinguished through microscopic images.

3.4. Hydrogen in grain boundary

To investigate how hydrogen permeation specifically affects the characteristics of the air side oxide layer, we used ToF-SIMS technology to capture two-dimensional images of hydrogen from single atmosphere and dual atmosphere samples exposed to 750 °C for 200 h in Fig. 5. The detected hydrogen signals may originate from atomic hydrogen, hydroxide ions, or other hydrogen-containing species, depending on their interaction with the oxide layer and surrounding environment. Prior to this, the sample was etched to expose the grain boundaries. To reduce errors, two-dimensional images are obtained within the same sputtering time interval and the same sputtering range. To visualize the grain boundaries, dashed lines were added to the image to illustrate the grain boundaries. Fig. 5(a) and (d) show SEM images of sputtering with clear grain boundaries. Fig. 5b and shows the two-dimensional image of the hydrogen distribution after ToF-SIMS testing, where the color contrast displays the changes in signal intensity and indicates the relative differences in concentration. The enhancement of image edge signals is an edge effect caused by the testing itself, and cannot indicate the enrichment of elements in that area [61]. Aside from this edge effect, no significant hydrogen enrichment was observed in the single atmosphere samples, particularly at the grain boundaries marked in Fig. 5(c). Additionally, no accumulation of hydrogen elements was detected.

However, in the two-dimensional image of the H distribution of the dual atmosphere sample in Fig. 5(e), in addition to the edge effect of the test itself, the intensity change of the signal can still be observed at the center of the image, that is, hydrogen is slightly higher in concentration at certain positions. Fig. 5(f) indicates the position of the grain boundary with dashed lines, and it is clearly observed that the location with high H concentration corresponds exactly to the grain boundary of the dual atmosphere sample. Therefore, it can be inferred that H from fuel measurement can diffuse into the interior of interconnect steel and accumulate at grain boundaries, which may be due to the lowest hydrogen evolution activation energy at grain boundaries and triple boundaries, which are the most favorable hydrogen evolution points [62,63]. Although the ToF-SIMS data clearly indicate hydrogen segregation at grain boundaries, the distribution of hydrogen was only captured after 200 h of exposure. Revealing the dynamic enrichment process of hydrogen may provide valuable directions for future comprehensive elucidation of hydrogen accumulation kinetics.

Yang et al. [64] provided an early analysis of the dual atmosphere effect from the perspective of hydrogen-doped oxide scales, suggesting that this mechanism accelerates oxide scale growth. According to the experiments of Skilbred et al. [65] and Alnegren et al. [17], the effect of hydrogen on the oxidation rate under dual atmosphere conditions can be estimated. Although the view that hydrogen is the main factor causing the dual atmosphere effect has been confirmed by many experimental results, there are still some studies that have the opposite effect. Ani et al. [66] believe that the effect of hydrogen on chromium diffusion in Fe–Cr alloys can be ignored. However, the diffusion coupling experiment at 800 °C only proved that hydrogen does not affect the lattice diffusion of chromium, and cannot explain the effect of hydrogen on the lattice diffusion of chromium. Gunduz et al. [19] inferred through Wagner's oxidation theory that the mechanism by which hydrogen affects the protective properties of chromium scales may be related to alleviating chromium migration at grain boundaries. Although there is no direct experimental evidence to prove that hydrogen affects chromium grain boundary diffusion, the hydrogen accumulation at the grain boundary in the dual atmosphere sample in this study makes this hypothesis more credible. The migration of chromium at grain boundaries may be restricted due to the adsorption of hydrogen on their inner surfaces, which in turn hinders chromium diffusion. However, in order to better understand the role of hydrogen in the migration of chromium through iron chromium alloys and the general dual atmospheric effect, further research is needed. DFT calculations may be helpful in understanding the diffusion effect of hydrogen on chromium.

3.5. Density functional theory computation

Based on the chromium concentration typically found in commercially available SUS430 ferritic alloys (16–18 wt% Cr) [26,27], a unit cell model of the Fe–Cr alloy (110) was established, containing 40 atoms (33 Fe, 7 Cr), as shown in Fig. 6(a). The crystal structure was visualized using the VESTA software. This model size was chosen to provide a balance between computational efficiency and accurate atomic-scale representation of Fe–Cr interactions.

The Fe unit cell, which has a Body-Centred Cubic (BCC) structure with Fm3 m symmetry, was optimized to obtain a lattice constant of 2.83 Å × 2.83 Å × 2.83 Å, which closely matches the experimental value of 2.867 Å [67]. The optimized unit cell was then used to construct a 2 × 2 × 5 supercell (40 atoms) with lattice parameters of 5.66 Å × 5.66 Å × 14.15 Å, allowing for a realistic simulation of Cr diffusion in a ferritic matrix.

The (110) surface was selected to create a slab model for studying the adsorption behavior of hydrogen and chromium diffusion because it is experimentally identified as the most abundant surface in SUS430, as evidenced by XRD analysis [68]. Furthermore, previous studies [69] have shown that the (110) surface has lower surface energy, making

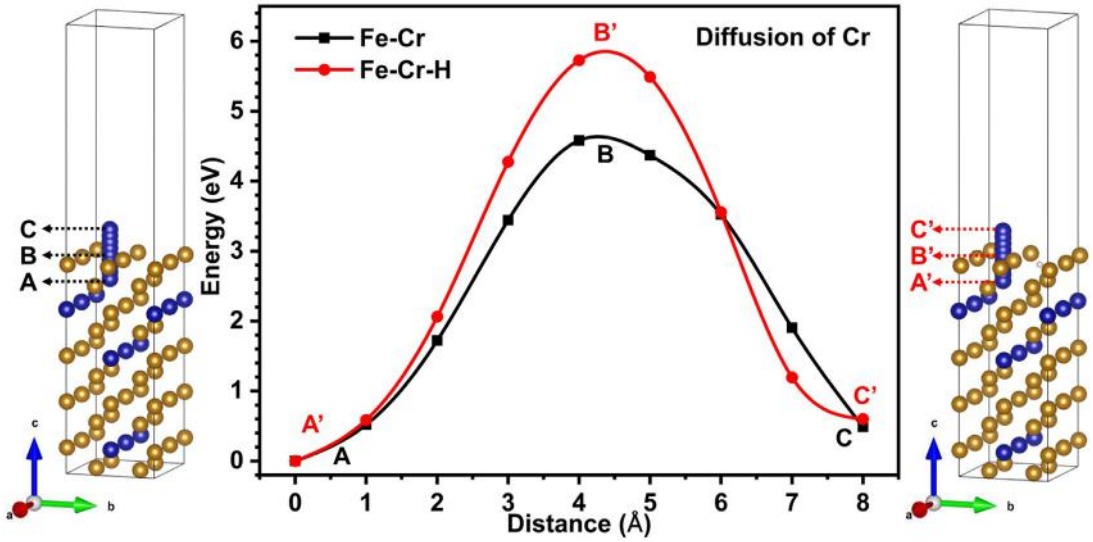


Fig. 7. The energy variation curve of diffusion path of Cr in Fe–Cr alloy. The black curve represents the Cr diffusion energy barrier (Fe–Cr) without hydrogen, while the red curve represents the Cr diffusion energy barrier (Fe–Cr–H) with hydrogen. The horizontal axis represents the distance of Cr diffusion path, and the vertical axis represents the energy at different positions during the diffusion process. (For interpretation of the references to color in this figure legend, the reader is referred to the web version of this article.)

it more stable and representative of real oxidation and adsorption processes in ferritic stainless steels.

To investigate the effect of hydrogen on chromium diffusion, a hydrogen atom was placed near the inner surface of the (110) slab to establish a hydrogen adsorption model, as shown in Fig. 6(b). Although our earlier analysis indicated that the detected hydrogen signals might originate from atomic hydrogen, hydroxide ions, or other hydrogen-containing species, our calculations focused solely on atomic hydrogen. This approach was chosen because atomic hydrogen is the most reactive form and can directly interact with metal atoms, influencing their diffusion characteristics. Additionally, simulating the effects of all possible hydrogen species would significantly increase computational complexity and resource requirements. Therefore, considering atomic hydrogen allows for a more direct and feasible assessment of its impact on chromium diffusion. The adsorption energy of hydrogen on the inner surface of (110) shown in the figure is −0.166 eV, indicating a spontaneous hydrogen adsorption at this location [70,71].

To study the diffusion characteristics of Cr in the two models, with and without hydrogen, the naked elastic band method [38] was used to calculate the diffusion energy barrier, as shown in Fig. 7. The diffusion pathway of Cr is displayed on the left and right sides respectively, with the starting point A (A′), the middle point B (B′), and the endpoint C (C′) of the diffusion pathway labeled. Cr and Fe atoms are represented by the blue and gold spheres, respectively. In the absence of hydrogen (Fe–Cr), the potential barrier energy for Cr diffusion is 4.4 eV. In the presence of hydrogen (Fe–Cr–H), the energy barrier for Cr diffusion significantly increases to 5.8 eV. After hydrogen was introduced, the activation energy required for Cr diffusion increased by approximately 1.4 eV. This indicates that the presence of hydrogen significantly increases the energy barrier for Cr diffusion [72,73].

The introduction of hydrogen increases the energy barrier on the diffusion pathway of Cr, which means that Cr atoms require more energy to overcome the potential barrier for diffusion [74]. This may be attributed to the interaction between hydrogen and surrounding atoms [75]. For example, hydrogen alters the local stress field or electronic structure of the crystal, increasing the resistance to Cr diffusion. Hydrogen may form stronger chemical bonds with certain sites in the diffusion pathway of Cr, stabilizing these sites and increasing the migration energy of Cr [76]. The inhibition of Cr diffusion by hydrogen may also lead to the complexity of the hydrogen embrittlement phenomenon, as hydrogen may play a “locking” role in the diffusion path [76,77].

It should be noted that the DFT model in this work represents a simplification of the actual complex scenario. While our discussion focuses on the effect of atomic hydrogen (H), the signals detected by ToF-SIMS include contributions from all hydrogen-containing species, such as H, OH^{-1}, and possibly others. Although atomic H is likely the primary factor contributing to embrittlement, the potential synergistic or competitive effects of other species should not be overlooked. Future studies combining in situ characterization with simulations of different hydrogen species will be essential to more accurately unravel the microscopic mechanisms of hydrogen-induced embrittlement.

4. Conclusion

In this study, the oxide layer formed under dual atmosphere conditions exhibits significant differences in thickness, composition, and morphology compared to that formed in a single atmosphere. Under dual atmosphere exposure, the oxide layer develops a stratified structure, consisting of an outer Fe_2O_3 layer growing outward, an inward-growing $(Fe, Cr)_3O_4$ layer beneath it, and continuous Cr_2O_3 bands at the metal-oxide interface. This layered structure indicates that the actual enrichment of chromium and inward oxidation lead to localized oxidation regions and cracks near the substrate material. The oxide layer reaches a thickness of approximately 37.0 μm. In contrast, after 200 h of oxidation in a single atmosphere, the sample forms a continuous oxide layer with a thickness of about 19.8 μm, primarily composed of Cr_2O_3, along with $FeMnFeO_4$ or Cr_2MnO_4 spinel phases.

The most significant distinction between the two atmospheres lies in the growth of Fe_2O_3, which may be linked to hydrogen enrichment at grain boundaries due to hydrogen diffusion from the anode side into the interconnect. This study evaluated hydrogen adsorption on the (110) Fe–Cr crystal plane and its effect on chromium diffusion using first-principles calculations. The results indicate that hydrogen increases the energy barrier for Cr diffusion, hinders Cr transport, weakens the protective role of Cr_2O_3, accelerates Fe diffusion, and ultimately exacerbates the degradation of the interconnect materials.

CRediT authorship contribution statement

Gongmei Yang: Writing – original draft, Methodology. **Siqi Wang:** Writing – review & editing, Software, Methodology. **Andrew Potter:** Writing – review & editing, Supervision. **Joy Sumner:** Writing – review & editing, Supervision.

Declaration of competing interest

The authors declare that they have no known competing financial interests or personal relationships that could have appeared to influence the work reported in this paper.

Acknowledgment

This research was supported by the Centre for Energy Engineering at Cranfield University (UK). Thanks to the China Scholarship Council (CSC) for providing living expenses. Data supporting this study are openly available from the following link:
https://doi.org/10.57996/cran.ceres-2731
https://dspace.lib.cranfield.ac.uk/handle/1826/2347.

Data availability

I have shared the link to my data in manuscript.

References

[1] A. Hauch, R. Küngas, P. Blennow, A.B. Hansen, J.B. Hansen, B.V. Mathiesen, M.B. Mogensen, Recent advances in solid oxide cell technology for electrolysis, Science 370 (6513) (2020) eaba6118.
[2] R.M. Ormerod, Solid oxide fuel cells, Chem. Soc. Rev. 32 (1) (2003) 17–28.
[3] L. Ye, K. Xie, High-temperature electrocatalysis and key materials in solid oxide electrolysis cells, J. Energy Chem. 54 (2021) 736–745.
[4] M.B. Mogensen, Materials for reversible solid oxide cells, Curr. Opin. Electrochem. 21 (2020) 265–273.
[5] J. Mao, E. Wang, H. Wang, M. Ouyang, Y. Chen, H. Hu, L. Lu, D. Ren, Y. Liu, Progress in metal corrosion mechanism and protective coating technology for interconnect and metal support of solid oxide cells, Renew. Sustain. Energy Rev. 185 (2023) 113597.
[6] N. Shaigan, W. Qu, D.G. Ivey, W. Chen, A review of recent progress in coatings, surface modifications and alloy developments for solid oxide fuel cell ferritic stainless steel interconnects, J. Power Sources 195 (6) (2010) 1529–1542.
[7] W. Junwei, L. Xingbo, Recent development of SOFC metallic interconnect, J. Mater. Sci. Technol. 26 (4) (2010) 293–305.
[8] J.W. Fergus, Metallic interconnects for solid oxide fuel cells, Mater. Sci. Eng.: A 397 (1–2) (2005) 271–283.
[9] S. Jiang, X. Chen, Chromium deposition and poisoning of cathodes of solid oxide fuel cells-a review, Int. J. Hydrog. Energy 39 (1) (2014) 505–531.
[10] L. Zhou, J.H. Mason, W. Li, X. Liu, Comprehensive review of chromium deposition and poisoning of solid oxide fuel cells (SOFCs) cathode materials, Renew. Sustain. Energy Rev. 134 (2020) 110320.
[11] M.J. Reddy, B. Kamecki, B. Talic, E. Zanchi, F. Smeacetto, J.S. Hardy, J.P. Choi, Ł. Mazur, R. Vaßen, S.N. Basu, et al., Experimental review of the performances of protective coatings for interconnects in solid oxide fuel cells, J. Power Sources 568 (2023) 232831.
[12] Z. Yang, M.S. Walker, P. Singh, J.W. Stevenson, T. Norby, Oxidation behavior of ferritic stainless steels under SOFC interconnect exposure conditions, J. Electrochem. Soc. 151 (12) (2004) B669.
[13] H. Kurokawa, Oxidation behavior of Fe–16Cr alloy interconnect for SOFC under hydrogen potential gradient, Solid State Ion. 168 (1–2) (2004) 13–21.
[14] J. Rufner, P. Gannon, P. White, M. Deibert, S. Teintze, R. Smith, H. Chen, Oxidation behavior of stainless steel 430 and 441 at 800 ° C in single (air/air) and dual atmosphere (air/hydrogen) exposures, Int. J. Hydrog. Energy 33 (4) (2008) 1392–1398.
[15] M. Ardigo, I. Popa, L. Combemale, S. Chevalier, F. Herbst, P. Girardon, Dual atmosphere study of the K41X stainless steel for interconnect application in high temperature water vapour electrolysis, Int. J. Hydrog. Energy 40 (15) (2015) 5305–5312.
[16] M. Stygar, T. Brylewski, A. Kruk, K. Przybylski, Oxidation properties of ferritic stainless steel in dual Ar-H_2-H_2O/air atmosphere exposure with regard to SOFC interconnect application, Solid State Ion. 262 (2014) 449–453.
[17] P. Alnegren, M. Sattari, J.-E. Svensson, J. Froitzheim, Temperature dependence of corrosion of ferritic stainless steel in dual atmosphere at 600-800 ° C, J. Power Sources 392 (2018) 129–138.
[18] C. Goebel, C. Bo, J.-E. Svensson, J. Froitzheim, The influence of different factors on the Dual Atmosphere effect Observed for AISI 441 interconnects Used in solid Oxide Fuel Cells, ECS Trans. 91 (1) (2019) 2261.
[19] K.O. Gunduz, A. Chyrkin, C. Goebel, L. Hansen, O. Hjorth, J.-E. Svensson, J. Froitzheim, The effect of hydrogen on the breakdown of the protective oxide scale in solid oxide fuel cell interconnects, Corros. Sci. 179 (2021) 109112.
[20] M. Stygar, T. Brylewski, A. Kruk, K. Przybylski, Oxidation properties of ferritic stainless steel in dual Ar-H_2-H_2O/air atmosphere exposure with regard to SOFC interconnect application, Solid State Ion. 262 (2014) 449–453.
[21] M. Tomas, J.-E. Svensson, J. Froitzheim, Evaluation of selected Fe–Cr steels under single-and dual-atmosphere conditions for intermediate-temperature solid oxide fuel cell interconnect applications, Int. J. Hydrog. Energy 65 (2024) 112–125.
[22] S. Yoneda, S. Abe, Y. Kawada, K. Imai, S. Hayashi, High-Temperature oxidation behavior of Fe-10Ni alloy in Air/Ar-H2-H2o dual atmosphere, in: Electrochemical Society Meeting Abstracts Prime2024, Vol. 14, The Electrochemical Society, Inc., 2024, p. 1594.
[23] J.C. Vickerman, ToF-SIMS—an overview, ToF-SIMS: Surf. Anal. Mass Spectrom. (2001) 1–40.
[24] M. Orio, D.A. Pantazis, F. Neese, Density functional theory, Photosynth. Res. 102 (2009) 443–453.
[25] P. Maragakis, S.A. Andreev, Y. Brumer, D.R. Reichman, E. Kaxiras, Adaptive nudged elastic band approach for transition state calculation, J. Chem. Phys. 117 (10) (2002) 4651–4658.
[26] H. Tsujimura, T. Goto, Y. Ito, Electrochemical surface nitriding of SUS 430 ferritic stainless steel, Mater. Sci. Eng.: A 355 (1–2) (2003) 315–319.
[27] Y. Shimomura, H.-W. Park, J. Yanagimoto, Hot deformation behavior of ferrite and austenite phases of ferritic stainless steel in the duplex temperature range, Mater. Sci. Eng.: A 923 (2025) 147698.
[28] P. Alnegren, M. Sattari, J.-E. Svensson, J. Froitzheim, Severe dual atmosphere effect at 600 ° C for stainless steel 441, J. Power Sources 301 (2016) 170–178.
[29] Y. Jiang, A.V. Virkar, Fuel composition and Diluent Effect on gas transport and performance of Anode-Supported SOFCs, J. Electrochem. Soc. 150 (7) (2003) A942.
[30] H. Yokokawa, H. Tu, B. Iwanschitz, A. Mai, Fundamental mechanisms limiting solid oxide fuel cell durability, J. Power Sources 182 (2) (2008) 400–412, Selected papers from the International Workshop on Degradation Issues in Fuel Cells.
[31] D.R. Gaskell, D.E. Laughlin, Introduction to the Thermodynamics of Materials, Sixth ed., Taylor & Francis, New York, 2017.
[32] A. Mazenc, A. Galtayries, A. Seyeux, P. Marcus, S. Leclercq, ToF-SIMS study of the behavior of thermally oxidized films formed on nickel-based 690 alloy in high-temperature water, Surf. Interface Anal. 45 (1) (2013) 583–586.
[33] M. Esmaily, P. Malmberg, M. Shahabi-Navid, J. Svensson, L. Johansson, A ToF-SIMS investigation of the corrosion behavior of Mg alloy AM50 in atmospheric environments, Appl. Surf. Sci. 360 (2016) 98–106.
[34] A. Seyeux, G. Frankel, N. Missert, K. Unocic, L. Klein, A. Galtayries, P. Marcus, ToF-SIMS imaging study of the early stages of corrosion in Al-Cu thin films, J. Electrochem. Soc. 158 (6) (2011) C165.
[35] X. Yue, P. Malmberg, E. Isotahdon, V. Ratia-Hanby, E. Huttunen-Saarivirta, C. Leygraf, J. Pan, Penetration of corrosive species into copper exposed to simulated O_2-free groundwater by time-of-flight secondary ion mass spectrometry (ToF-SIMS), Corros. Sci. 210 (2023) 110833.
[36] T. Brylewski, M. Nanko, T. Maruyama, K. Przybylski, Application of Fe–16Cr ferritic alloy to interconnector for a solid oxide fuel cell, Solid State Ion. 143 (2) (2001) 131–150.
[37] P. Giannozzi, S. Baroni, N. Bonini, M. Calandra, R. Car, C. Cavazzoni, D. Ceresoli, G.L. Chiarotti, M. Cococcioni, I. Dabo, et al., QUANTUM ESPRESSO: a modular and open-source software project for quantum simulations of materials, J. Phys.: Condens. Matter. 21 (39) (2009) 395502.
[38] H. Jónsson, G. Mills, K.W. Jacobsen, Nudged elastic band method for finding minimum energy paths of transitions, in: Classical and Quantum Dynamics in Condensed Phase Simulations, World Scientific, 1998, pp. 385–404.
[39] J. Tien, F. Pettit, Mechanism of oxide adherence on Fe-25Cr-4Al (Y or Sc) alloys, Met. Trans. 3 (1972) 1587–1599.
[40] H. Hindam, D. Whittle, Microstructure, adhesion and growth kinetics of protective scales on metals and alloys, Oxid. Met. 18 (5) (1982) 245–284.
[41] R.L. Tollman, E.A. Gulbransen, Crystal morphology and mechanisms of growth of alpha-Fe_2O_3 whiskers on iron, J. Electrochem. Soc. 114 (12) (1967) 1227.
[42] R. Spotorno, D. Paravidino, S. Delsante, P. Piccardo, Volatilization of chromium from AISI 441 stainless steel: Time and temperature dependence, Surf. Coat. Technol. 433 (2022) 128125.
[43] A. Sabioni, A. Huntz, L. Borges, F. Jomard, First study of manganese diffusion in Cr_2O_3 polycrystals and thin films by SIMS, Phil. Mag. 87 (12) (2007) 1921–1937.
[44] H. Graham, H. Davis, Oxidation/vaporization kinetics of Cr_2O_3, J. Am. Ceram. Soc. 54 (2) (1971) 89–93.
[45] T. Jonsson, B. Pujilaksono, H. Heidari, F. Liu, J.-E. Svensson, M. Halvarsson, L.-G. Johansson, Oxidation of Fe-10Cr in O_2 and in O_2+H_2O environment at 600 ° C: A microstructural investigation, Corros. Sci. 75 (2013) 326–336.

[46] F. Stott, G. Wood, Internal oxidation, Mater. Sci. Technol. 4 (12) (1988) 1072–1078.
[47] P. Hou, J. Stringer, The effect of reactive element additions on the selective oxidation, growth and adhesion of chromia scales, Mater. Sci. Eng.: A 202 (1–2) (1995) 1–10.
[48] A. Kahveci, G. Welsch, Oxidation of Fe-3 wt.% Cr alloy, Oxid. Met. 26 (1986) 213–230.
[49] C. Goebel, P. Alnegren, R. Faust, J.-E. Svensson, J. Froitzheim, The effect of pre-oxidation parameters on the corrosion behavior of AISI 441 in dual atmosphere, Int. J. Hydrog. Energy 43 (31) (2018) 14665–14674.
[50] S. Qi, N. Porotnikova, M. Ananyev, A. Kuzmin, V. Eremin, A. Pankratov, N. Molchanova, O. Reznitskikh, A. Farlenkov, E. Vovkotrub, et al., High-temperature glassy-ceramic sealants SiO_2-Al_2O_3-BaO-MgO and SiO_2-Al_2O3-ZrO_2-CaO-Na_2O for solid oxide electrochemical devices, Trans. Nonferr. Met. Soc. China 26 (11) (2016) 2916–2924.
[51] B. Pujilaksono, T. Jonsson, H. Heidari, M. Halvarsson, J.-E. Svensson, L.-G. Johansson, Oxidation of binary FeCr alloys (Fe-2.25Cr, Fe-10Cr, Fe-18Cr and Fe-25Cr) in O_2 and in O_2+H_2O environment at 600 ° C, Oxid. Met. 75 (2011) 183–207.
[52] G.C. Wood, High-temperature oxidation of alloys, Oxid. Met. 2 (1) (1970) 11–57.
[53] G. Wood, D. Whittle, The mechanism of breakthrough of protective chromium oxide scales on Fe-Cr alloys, Corros. Sci. 7 (11) (1967) 763–782.
[54] D. Young, J. Zurek, L. Singheiser, W. Quadakkers, Temperature dependence of oxide scale formation on high-Cr ferritic steels in Ar-H_2-H_2O, Corros. Sci. 53 (6) (2011) 2131–2141.
[55] A. Rahmel, J. Tobolski, Einfluss von wasserdampf und kohlendioxyd auf die oxydation von eisen in sauerstoff bei hohen temperaturen, Corros. Sci. 5 (5) (1965) 333–346.
[56] X. Peng, J. Yan, Y. Zhou, F. Wang, Effect of grain refinement on the resistance of 304 stainless steel to breakaway oxidation in wet air, Acta Mater. 53 (19) (2005) 5079–5088.
[57] J. Zhan, Y. Yang, H. Bi, M. Li, H. Gu, High temperature oxidation behavior of type 444 stainless steel in synthetic automotive exhaust gas, J. Mater. Res. Technol. 12 (2021) 530–541.
[58] F. Liu, J.E. Tang, T. Jonsson, S. Canovic, K. Segerdahl, J.E. Svensson, M. Halvarsson, Microstructural investigation of protective and non-protective oxides on 11% chromium steel, Oxid. Met. 66 (2006) 295–319.
[59] X. Cheng, Z. Jiang, D. Wei, J. Zhao, B.J. Monaghan, R.J. Longbottom, L. Jiang, Characteristics of oxide scale formed on ferritic stainless steels in simulated reheating atmosphere, Surf. Coat. Technol. 258 (2014) 257–267.
[60] S. Yen, Y. Tsai, Critical hydrogen concentration for the brittle fracture of AISI 430 stainless steel, J. Electrochem. Soc. 143 (9) (1996) 2736.
[61] R.N. Sodhi, Time-of-flight secondary ion mass spectrometry (TOF-SIMS): versatility in chemical and imaging surface analysis, Analyst 129 (6) (2004) 483–487.
[62] N. Yazdipour, A. Haq, K. Muzaka, E.V. Pereloma, 2D modelling of the effect of grain size on hydrogen diffusion in X70 steel, Comput. Mater. Sci. 56 (2012) 49–57.
[63] Y. He, Y. Su, H. Yu, C. Chen, First-principles study of hydrogen trapping and diffusion at grain boundaries in γ-Fe, Int. J. Hydrog. Energy 46 (10) (2021) 7589–7600.
[64] Z. Yang, M.S. Walker, P. Singh, J.W. Stevenson, Anomalous corrosion behavior of stainless steels under SOFC interconnect exposure conditions, Electrochem. Solid-State Lett. 6 (10) (2003) B35.
[65] A.W.B. Skilbred, R. Haugsrud, The effect of dual atmosphere conditions on the corrosion of Sandvik Sanergy HT, Int. J. Hydrog. Energy 37 (9) (2012) 8095–8101.
[66] M.H.B. Ani, T. Kodama, M. Ueda, K. Kawamura, T. Maruyama, The effect of water vapor on high temperature oxidation of Fe-Cr alloys at 1073K, Mater. Trans. 50 (11) (2009) 2656–2663.
[67] A. Subagyo, H. Oka, G. Eilers, K. Sueoka, K. Mukasa, Scanning tunneling microscopy observation of epitaxial bcc-Fe (001) surface, Japan. J. Appl. Phys. 39 (6S) (2000) 3777.
[68] Y. Yu, S. Shironita, K. Souma, M. Umeda, Effect of chromium content on the corrosion resistance of ferritic stainless steels in sulfuric acid solution, Heliyon 4 (11) (2018).
[69] E. Aghemenloh, J. Umukoro, S. Azi, S. Yusuf, J. Idiodi, Surface energy calculation of bcc metals using the analytical equivalent crystal theory method, Comput. Mater. Sci. 50 (12) (2011) 3290–3296.
[70] P. Bruzzoni, R.C. Pasianot, A DFT study of H solubility and diffusion in the Fe-Cr system, Comput. Mater. Sci. 154 (2018) 243–250.
[71] Y. Sun, Y.F. Cheng, Thermodynamics of spontaneous dissociation and dissociative adsorption of hydrogen molecules and hydrogen atom adsorption and absorption on steel under pipelining conditions, Int. J. Hydrog. Energy 46 (69) (2021) 34469–34486.
[72] L. Wang, W. Yang, Z. Ma, J. Zhu, Y. Li, First-principles study of chromium diffusion in the ferritic Fe-Cr alloy, Comput. Mater. Sci. 181 (2020) 109733.
[73] Y. Zhang, W. Qiao, W. Li, K. Li, W. Wang, V.R. Misko, W. Yang, Cr diffusion at the FeCr/Cr_2O_3 interface: A first-principles study, Comput. Mater. Sci. 230 (2023) 112511.
[74] Y. Zhu, L. Fang, Z. Zeng, X. Wang, Ultrahigh hydrogen diffusivities in Al_2O_3 under high pressure, Phys. Rev. B 110 (14) (2024) 144310.
[75] B. Tveten, G. Hultquist, T. Norby, Hydrogen in chromium: influence on the high-temperature oxidation kinetics in O_2, oxide-growth mechanisms, and scale adherence, Oxid. Met. 51 (3) (1999) 221–233.
[76] K. Hirata, S. Iikubo, H. Ohtani, First-principles calculations of the effects of Mn, Cr, and Ni on hydrogen diffusion in BCC, FCC, and HCP Fe, Tetsu-To-Hagane/J. Iron Steel Inst. Jpn. 105 (2) (2019) 109–117.
[77] Y. Fukai, H. Sugimoto, Diffusion of hydrogen in metals, Adv. Phys. 34 (2) (1985) 263–326.



https://dspace.org/

Investigating the role of grain boundary hydrogen in dual atmosphere effects for solid oxide cells interconnect applications

Yang, Gongmei; Wang, Siqi; Potter, Andrew; Sumner, Joy

2026-01-01
Elsevier
https://doi.org/10.1016/j.corsci.2025.113333
Yang G, Wang S, Potter A, Sumner J. (2025) Investigating the role of grain boundary hydrogen in dual atmosphere effects for solid oxide cells interconnect applications. Corrosion Science, Volume 258, January 2026, Article number 113333

Downloaded from a DSpace repository. https://dspace.org/